Journal of *Marine Science and Engineering*

MDPI

Article

Experimental and Numerical Investigation of Floating Large Woody Debris Impact on a Masonry Arch Bridge

Eda Majtan *, Lee S. Cunningham and Benedict D. Rogers

Department of Mechanical, Aerospace and Civil Engineering, The University of Manchester, Manchester M13 9PL, UK; lee.scott.cunningham@manchester.ac.uk (L.S.C.); benedict.rogers@manchester.ac.uk (B.D.R.)

* Correspondence: eda.arikan@manchester.ac.uk

Abstract: Masonry arch bridges form an essential part of existing transport infrastructure around the world, including mainland Europe and the northeastern US. Recent extreme flood events highlight that masonry arch bridges spanning watercourses are vulnerable to flood-induced hydrodynamic and debris impact loads. When the flow interacts with the bridge superstructure, with or without discrete floating debris, a complex interaction is observed. This paper presents both experimental and numerical studies to investigate this complex phenomenon, including fluid–structure and structure–structure interactions. A typical single-span masonry arch bridge and large woody debris representing a tree log are investigated. Experimental observations from a scaled hydraulic model, with and without debris in the flow, are first presented for the case where the abutment of the bridge is fully submerged. Next, the capability of the numerical method smoothed particle hydrodynamics (SPH) in simulating the hydrodynamic behaviour and debris impact observed in the experiment is discussed. Following this, both hydrodynamic and debris-induced pressure–time histories on the bridge are obtained using the SPH model. Results reveal that the debris impact leads to a significantly more localised load on the bridge compared to the situation with hydrodynamic load only.

Keywords: masonry arch bridges; flood events; open channel flow; discrete debris impact force; drag force; pressures; SPH

Citation: Majtan, E.; Cunningham, L.S.; Rogers, B.D. Experimental and Numerical Investigation of Floating Large Woody Debris Impact on a Masonry Arch Bridge. *J. Mar. Sci. Eng.* **2022**, *10*, 911. https://doi.org/10.3390/jmse10070911

Academic Editors: Majid Mohammadian, Denis Istrati, Ian Buckle and Michael Scott

Received: 29 April 2022
Accepted: 28 June 2022
Published: 1 July 2022

1. Introduction

Bridges are an essential part of our infrastructure and can be damaged or destroyed by flooding, as observed in many places around the world. Floods caused damage to or collapsed 28 bridges in 1952 in Lynmouth, UK, 233 bridges in 1976 in Japan and 73 bridges in 1985 in the US [1]. The 2002 flood in Central Europe caused damage and/or collapse of several hundred bridges in Germany [2] and the Czech Republic [3]. Serious flood damage to bridges was seen in Boscastle, UK, in August 2004 [4], in the US in August 2005 after Hurricane Katrina [5], in Cumbria, UK, in November 2009, in Afghanistan in 2012 [2] and in the UK in December 2015 after storms Desmond and Eva [6].

Masonry arch bridges are among the oldest bridge types and date back several thousand years. Although masonry arch construction became less popular towards the early part of the 20th century due to associated labour costs and the emerging technology of steel and concrete, this bridge form still constitutes a vital part of transport infrastructure networks worldwide. It is estimated that between 200,000 and 500,000 masonry arch bridges are in daily use in mainland Europe [7,8]. Approximately 35,000 in Germany, 78,000 in France, 56,800 in Italy and 17,867 in the UK are in the use of railway networks alone; the overall number is approximately 40,000 in the UK [9]. Existing masonry arch bridges show good performance under normal service loads; however, extreme environment loading with possible deterioration and ageing over time may limit the performance of these bridges spanning watercourses. A number of masonry arch bridges have been damaged or

destroyed during the extreme flood events in the last two decades; some examples in the UK are given by Majtan et al. [6]. The damage and failure of masonry arch bridges causes disruption to transportation networks, communities and services; for example, Figure 1 shows a brickwork road bridge in Derbyshire, UK which was closed due to damage (ring separation and bulging of the spandrel wall) and requires remedial works to continue its service.

Figure 1. Downstream elevation of a single-span brickwork arch bridge spanning Bollinhurst Brook in Lyme Park, Cheshire, UK, with woody debris located upstream and damage at the spandrel wall and arch barrel (image by Eda Majtan).

To assess these existing bridges in flood risk areas, the flood-induced loads on masonry arch bridges need to be quantified. These hydraulic actions at existing highway bridges are considered by the UK's National Highways' assessment code (CS 469, formerly BD 97/12) [10,11]; however, the main focus is the identification of scour effects and associated substructure behaviour of the bridge. Diehl [12] performed a detailed study to predict debris accumulation at bridges and US NCHRP report 445 [13] investigated debris forces on bridges with different drag coefficients associated with the flow–blockage ratio. However, none of these guidance or design codes [10,14,15] focused on masonry arch bridges and no specific equations for calculating forces on this bridge form are available [16]. Flood-induced loads on the structural components of a masonry arch bridge (abutment, arch barrel, spandrel wall) are different from those of other bridge forms, considering its geometry and structural behaviour.

Flood-induced loads on a masonry arch bridge can be categorised as: horizontal hydrostatic force, horizontal hydrodynamic (drag) force, hydrodynamic uplift force, hydrostatic uplift force where the arch barrel and backfill are submerged and floating debris impact and accumulation (Figures 1 and 2). Guidance on calculating hydrodynamic (drag) and uplift forces on the superstructure with simple geometry can be found in Australia's bridge design standard [15], the UK's National Highways' design code [14] and the US's Federal Highway Administrations' report [17]. Since a masonry arch bridge crossing a waterway is either partially or entirely submerged by the water during flood events, the bridge is subject to a hydrostatic uplift force, i.e., a buoyancy force depending on the submergence ratio. The buoyancy force mainly equates to the differences in hydrostatic pressures exerted on the bottom and top of the deck submerged in water that can be calculated in relation to the displaced volume of the submerged deck and density difference. As Robertson et al. [18] concluded for concrete decks, submergence in water decreases the effective self-weight of the structural members by nearly 50%. This type of reduction in the effective self-weight due to buoyancy results in decreasing the compressive stresses of the main load-carrying

member of masonry arch bridges, the arch barrel. Considering this change in the stress state, the bridge may become more prone to failure.

Figure 2. Debris accumulation at the bridge cutwater (the streamlined head of the bridge pier) in the River Wye in Derbyshire, UK (Image by Eda Majtan).

In addition, single or multiple pieces of large floating debris and accumulations of floating debris (e.g., leaves, wood and other objects lighter than water) around masonry arch bridges in rivers are an important problem [19,20]. This may result in a decrease in the capacity of bridge openings, thus causing an increase in the backwater upstream of the bridge, as well as the distribution of the hydrodynamic forces on the bridge superstructure with increase in water level. In addition to these increased lateral forces on the structural components of bridges with the presence of the debris, the debris impact loading on the structures may be highly transient since they are occurring in a shorter time compared to the hydrodynamic forces. Although the importance of this loading type has been emphasised by the studies associated with tsunami-induced loads on other structures [21–23] and the first numerical study performed by Majtan et al. [6] to investigate the flood-induced loads on arch bridges spanning watercourses, there is no experimental study in the literature of this nature. Considering this gap in the assessment codes as well as the research literature, the present study explores these flood-induced loads on a single-span masonry arch bridge both experimentally and numerically. The work presented here forms part of a more extensive experimental campaign, the full extent of which, including the dynamic characterization of the test assembly, is discussed in a forthcoming separate publication.

To decide an optimal numerical modelling approach in relation to this complex phenomenon including both fluid–structure and structure–structure interaction, most common mesh-based (Eulerian) and meshless (Lagrangian) computational fluid dynamics (CFD) methods are discussed herein. Three mathematical models of mesh-based CFD methods, finite difference method (FDM), finite volume method (FVM) and finite element method (FEM), are employed in the literature depending on the target application, with different initial conditions, boundary conditions and the set of partial differential equations, etc. Although the FDM can obtain higher-order accuracy without any truncation errors on structured meshes, it cannot be employed in most engineering problems with complex geometries [24]. The FEM is the most commonly used method for solid mechanics problems, and it has been successful in estimating tsunami-induced hydrodynamic loads on bridge decks [25], along with the particle finite element method (PFEM) [26]. However, the method suffers from the drawbacks of mesh generation and remeshing required for complex highly nonlinear flows. Xiang et al. [27] recently applied the Arbitrary Lagrangian-Eulerian formulation of the FEM to investigate tsunami-induced wave impact on bridges; however, mesh generation may still be problematic, with a complex geometry. Although the FVM

was successfully applied in fluid mechanics, modelling the interface and/or interfacial phenomena, i.e., multi-phase flows, free-surface flows and fluid–structure interaction, is the most challenging part [28].

To treat the interfacial flows that exist in multi-phase phenomena, a volume-of-fluid (VOF) method was developed [28]. This method aims to track the motion of the free surface in time which still requires a CFD solver (i.e., FVM, FEM) to solve differential equations. Although this approach was usually used by various computer codes to solve fluid–structure interaction problems where free surface is involved, such as ANSYS Fluent, FLOW-3D and OpenFOAM [29–35], tracking a floating debris and associated structure–structure interaction phenomena continues to be a challenge. The difficulties of applying the conventional mesh-based methods resulted in developing meshless particle (Lagrangian) methods in order to tackle the problems with a deformable boundary, moving interface and free surface. The lattice Boltzmann method (LBM) calculates a fluid density on a lattice with streaming and relaxation (collision) processes rather than solving Navier–Stokes equations [36,37]. The method can treat the interfacial flows easily with its natural ability, whereas the reliability of the physical models for inter-particle force representation and flow viscosity is the main concern. Additionally, modelling interfacial jump conditions with the presence of surface tension, high viscosity ratio and density is challenging [28]. The moving particle semi-implicit (MPS) and smoothed particle hydrodynamics (SPH) methods obtain a realistic physical modelling of interface problems in the meshless particle methods. Although both methods approximate the strong form of the partial differential equations based on integral interpolants, the MPS method employs a simplified differential operator depending on a local weighted averaging procedure, rather than the gradient of a kernel function used in the SPH method. Another difference between the methods is the solution process of partial differential equations. The MPS uses a semi-implicit prediction-correction approach, compared to the fully explicit approach widely used in SPH. Though both methods can be employed on interfacial problems successfully [38,39], SPH has received more attention by researchers, hence offers more advanced methodologies appropriate for the present research, e.g., open boundary conditions and a floating object. Although the standard SPH method has shortcomings similar to the other CFD methods, e.g., simulating the interface with large ratios of density/viscosity discontinuity and approximating flow variable accurately as an optimised point between the numerical diffusion and interpolation accuracy, the recent modifications, such as delta-SPH, particle shifting and kernel gradient corrections, enable tackling these problems by evaluating the accuracy, convergence and efficiency of the SPH method [40–44]. It should also be noted that whilst the present study focuses on a discrete piece of floating debris impacting a structure using a one-way coupling, previous studies have explored interactions between multiple debris in a flow field as well as fixed structures by coupling various numerical approaches, e.g., discrete element method and FEM [39,45–49]. The authors' wider research investigates the structural response of masonry arch bridges subject to these loads.

Considering the gap highlighted above, this paper first presents an experimental investigation of flood-induced hydrostatic, hydrodynamic and discrete floating debris (representing a tree log) impact loads on a single-span arch bridge (1:10 scale) where the abutment was fully submerged. Then, the capability of the SPH model to capture this complex phenomenon is evaluated in terms of velocity, water elevation and force using the open-source DualSPHysics v5.0 code. Following this, spatial pressure distributions on the bridge and associated pressure–time histories in the cases with and without debris are obtained using the SPH model. Finally, the main findings and limitations in both the experiment and the SPH numerical model are discussed.

2. Experimental Investigation

2.1. Experimental Setup

The hydraulic experiments were carried out using an existing recirculating flume at the University of Manchester. The flume is 4.88 m long, 1.22 m wide and 0.61 m high

without any slope, as shown schematically in Figure 3. The flume test section was kept to a section of the flume 2.88 m in length between location V1 and the outlet. A perforated metal plate at the inlet was used to eliminate possible unwanted objects in the test area, whilst a rectangular piece of wood acted as the weir at the outlet. The arch bridge was modelled with 1:10 scale in the experiment with a 0.8 m span, 0.25 rise-to-span ratio and 0.4 m width in the flow direction. Similar to previous hydraulic experiments [50,51], a fairly rigid and transparent arch bridge was constructed using 12 mm thick acrylic Perspex. It should be noted that in the corresponding SPH model, the arch is assumed to be fully rigid; this is obviously a simplification. Considering the presence of the debris and unknown location of the debris impact, the bridge was suspended keeping an approximately 5 mm gap between the flume surface and bridge bottom (Figure 3a). Similarly, the abutment dimension perpendicular to the flow direction was 0.205 m to keep the gap of 5 mm between the flume side wall and bridge side wall, so that the bridge was allowed to freely move in the flow direction under hydrodynamic and debris impact forces (Figure 3b). In theory, the bridge is free to move in the direction of the flow; however, the load cell immediately adjacent to the downstream face is fixed in order to measure the reaction force resulting from the hydrodynamic flow and debris impact on the bridge. The equivalent full-scale bridge height of 4.5 m was decided in consideration of common rise-to-span ratios [52], backfill depth at the crown, as well as the parapet wall height of the bridge. With a 1:10 scale model, this equates to 0.45 m height of the modelled bridge. To represent a tree log in the rivers (Figure 2), a cylindrical debris was designated based on the span length of the bridge and the ratio between the length and diameter of the debris with 0.059, based on several studies [53–55]. In reality, tree logs are likely to incorporate branches, etc., which may have an effect on behaviour; however, this is outside the scope of the present study. Locations V1–V9 in the flume test section (Figure 3a) represented the measurement points for both velocity and height. Froude scaling was used throughout the experiment [56].

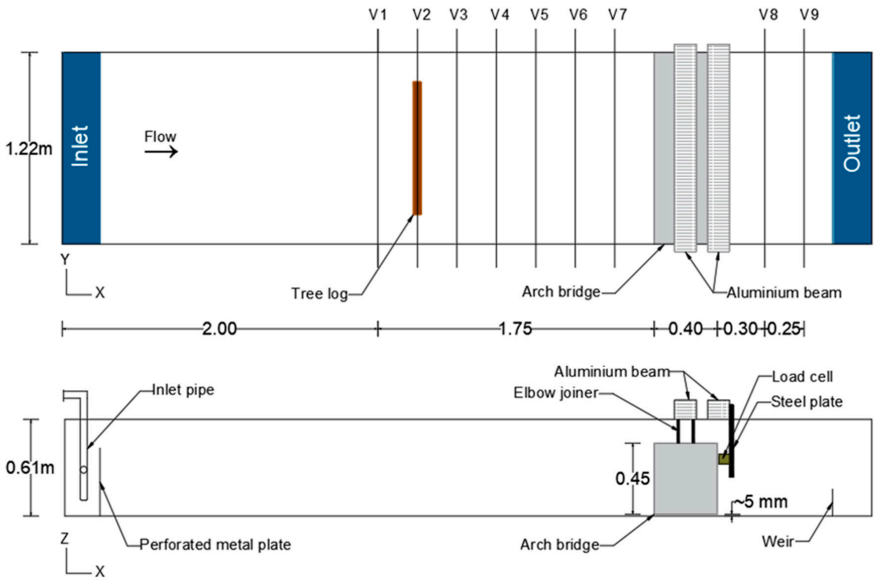

(**a**) Plan and side view of experimental setup

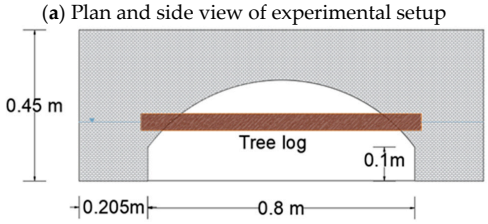

(**b**) Cross-section of a single-span arch bridge

Figure 3. (**a**) Plan and side view of experimental setup with the velocity and water depth measurement locations of V1–V9 (not to scale) and (**b**) cross-section of a single-span arch bridge with tree log.

To suspend the bridge, four elbow joiners were used where movement was only allowed in the flow direction and restraint provided in other directions (Figure 4). Behind the bridge, on the downstream side, another beam was mounted to carry the steel plates and load cells used. The locations of the steel beams and load cells were parallel with respect to the longitudinal centreline of the bridge. The most important point here was to keep the distance between two aluminium beams used for the bridge and load cells the same.

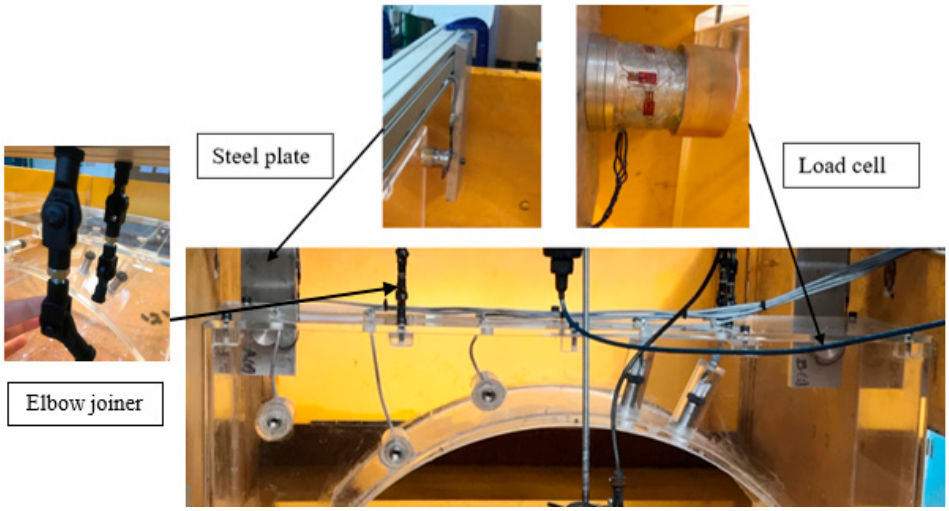

Figure 4. Image of suspended bridge and load cell installation.

2.2. Test Cases and Data Acquisation

The hydraulic conditions in the experiments were set based on the flume capacity in terms of the flow rate where the water depth at the V1 location was 0.208 m for the fully submerged abutment, and the free-surface velocity was kept as approximately 0.2 m/s corresponding to the flow rate of 0.0436 m^3/s. This was the main limitation of the experiment, where the geometrical similarity based on Froude scaling was successfully achieved, whilst the kinematics of a real flooding scenario could not be replicated, considering the free-surface velocity of 0.67 m/s in the prototype compared to those observed during the real floods, e.g., approximately 3.14 m/s at Pooley Bridge, 3.2 m/s at Eamont Bridge, 4.2 m/s at Brougham Bridge and 4.3 m/s at Sprint Bridge during the 2015 UK flood events [57]. The focus of the experiment was to obtain the ratio between the loads without and with debris (Table 1), as well as to provide data for validation purposes detailed in Section 3. Further investigation, e.g., possible yaw and overturning moment measurements may be performed in future studies [58]. The most common floating debris type in watercourses [6], a tree log, specifically English Brown Oak with a density of 905 kg/m^3 (wet) was used in case 2. The length and diameter of this cylindrical debris were 0.84 m and 0.05 m representing a tree log with the diameter–length ratio of 0.059. The initial debris orientation was defined as the orientation of debris at V2 location representing 1.5 m upstream of the bridge with regard to its centre of mass, where the long axis of the debris was parallel to the bridge span. It should be noted that a set of 5 experimental runs for each case was performed as a part of repeatability analysis and further discussions on the accuracy of the measurements are provided in the following section.

Table 1. Details of case studies.

Case	Flow Depth at V1 (m)	Flow Rate (m^3/s)	Fr	Re	Debris
1	0.208	0.0436	0.120	35,724	-
2	0.208	0.0436	0.120	35,724	Tree log

The streamwise, vertical and spanwise velocities of water were measured at locations V1–V9 using Nortek Vectrino Acoustic Doppler Velocimeter (ADV). The sampling rate of 200 Hz was employed for all velocity measurements considering previous experiments performed using the same flume with a similar hydraulic condition [59]. Additionally, it should be noted that a fast sampling rate may cause higher variability in the velocity measurement, with an increase in the standard deviation [60]. To obtain an accurate velocity measurement at the free-surface level without fluctuation, glass microspheres were added at 1 m upstream of the measurement point. To optimise the time period for recording velocity, as well as the accuracy, a time period of 60 s was chosen equating to 12,000 total velocity measurements with 200 Hz for each case with maximum difference of 2.52% in the results, compared to a longer time period of 120 s. The input module with two channels, the NI-9218, was connected to the NI Data Acquisition (DAQ) system not only to read but also to adapt the load cell outputs comprising full-bridge strain gauges. An NI cDAQ-9178 driver was used in this experiment. After setting up all data-logging devices, the DAQ system was connected to the computer where the LabVIEW software was programmed accordingly. With the presence of debris resulting in short-time debris impact forces on the bridge, the sampling frequency needed to be at least 500 Hz to be able to capture these short-time impulsive forces, based on the preliminary SPH numerical results [6]. Following the Nyquist–Shannon sampling theorem, the sampling frequency was kept higher than the minimum required to retain all information without missing any data [61]. A sampling rate of 2000 Hz was therefore employed in the experiments. Although the sampling rate could have been increased within the programmable LabVIEW software, this optimal value was used with regard to the amount of required memory with higher sampling rate.

The debris motion was recorded using a Panasonic Lumix DMC-TZ71 camera at the side of the flume (Figure 5a). Videos of each test run were recorded at 50 frames per second (fps) with a resolution of 1920 × 1080 pixel. A video editor (Movavi) was used to adjust the frame rate and resolution if necessary, as well as to capture debris motion. Every 0.1 m with the total of 0.3 m upstream of the bridge was marked (Figure 5b) in order to estimate the debris velocity at the impact location by using the time from the videos recorded. Although no bias was observed in the flume based on preliminary experiments, the debris orientation at the impact location varied in the tests of each case. This might be due to human errors, considering no mechanical system was used for releasing the debris inside the water flow.

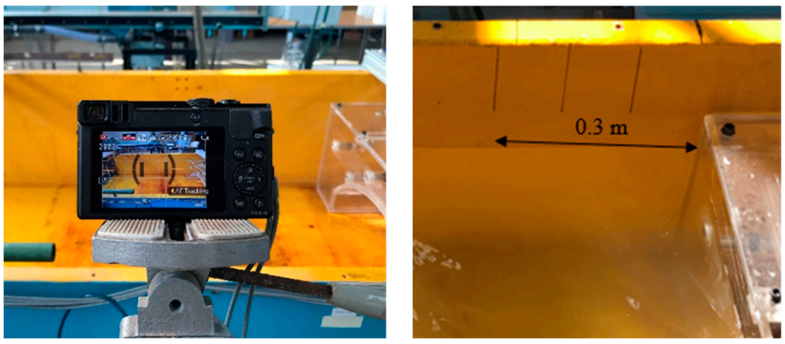

(**a**) (**b**)

Figure 5. (**a**) Camera used in the experiment and (**b**) marked locations upstream of the bridge.

2.3. Results

This section presents the results obtained from the experiment. The results in relation to kinematics of the water flow are first discussed with the water level and depth-averaged velocity at these V1–V9 locations. Then, the dynamics of the flow and debris carried by the flow around the bridge is examined with the force values. Further discussion on the results of related uncertainty and statistical analyses is also provided in the associated sections.

2.3.1. Flow Depths and Depth-Averaged Velocity Profiles

The free-surface and flume bottom levels were measured using a water depth gauge so as to obtain the water depth at the lateral centreline of the locations V1–V9. The water depth at the location V1 was 0.208 m with the 0.1 m-high weir at the outlet, 0.75 m downstream of the bridge rear wall. Figure 6a illustrates the water level elevations through the flume centreline in case 1 upstream and downstream of the bridge, regardless of the bridge width in the flow direction The measurement was taken every 0.25 m upstream representing with V1–V7, while the V8 was 0.3 m downstream of the bridge, due to the presence of the second aluminium beam used for the load cells, and the distance between V8 and V9 was 0.25 m. Repeatability analysis was conducted for each case to be able to provide the same hydraulic conditions, since a small instability occurred in this water depth, and velocity measurements related to the kinematics of the flow can nonetheless cause a significant scatter in pressure and force records [62,63]. Based on the analysis, the uncertainty of ±1.5 mm was observed in the water depth measurements.

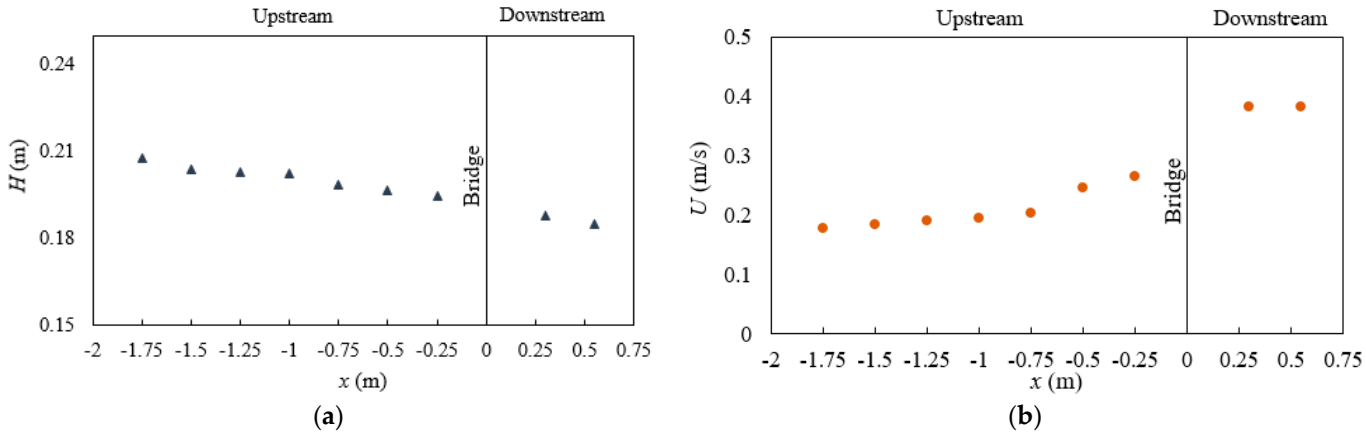

Figure 6. (**a**) Water surface elevations and (**b**) depth-averaged velocity profile in the x direction at the lateral centreline of the flume in case 1.

The fluid velocity tangential to the boundary goes to zero at the solid boundary. This phenomenon is called the no-slip condition, where the fluid velocity matches the boundary velocity (zero in the experiment) owing to the friction effect of the flume walls and bottom. In accordance with this, the water velocity decreased near the bed of the flume in the experiment, while the velocity reached the highest value at the free-surface level and the velocity varied over the vertical coordinate between the bed and free surface. This spatial variation of velocity, called shear, affects the boundary layer next to the walls and bed. The height of the boundary layer is theoretically defined as the distance above the bed where the local velocity reaches 99% of free-stream velocity. This can vary with different viscosity values associated with the bed characteristics. To minimise the effects of not only this variation, but also possible human errors in taking the measurement, and hence reduce uncertainty in the measurements, the depth-averaged velocity profiles were produced. Ten readings along the water depth in the z direction were obtained at the centreline of the location V1–V9 for each case with an uncertainty of ±0.008 m/s. Then these local velocity values were used to calculate the depth-averaged velocities at those locations. Figure 6b illustrates the depth-averaged velocity profile in the x direction at the flume centreline with a depth-averaged velocity of 0.1784 m/s at V1 and 0.3815 m/s at V9. When the flow is constricted due to the presence of the bridge, the depth-averaged velocity at the bridge opening increases to maintain the constant flow rate.

2.3.2. Hydrodynamic and Debris Impact Loads

To characterise the confidence intervals of the peak pressure and force value, as well as their repeatability from one experiment to another, five experiments were carried out for each case, referred to as R1 to R5. Figure 7a shows an image of the free-surface level

around the bridge observed in the first reading in case 1 with a fully submerged abutment. The results of each test are provided in Figure 7b, where the force in the graphs represents the total force corresponding to the drag force in case 1 with hydrodynamic load only, and total force (drag force and debris impact force) with case 2 with the presence of the debris. This facilitated obtaining the confidence interval, as well as detailed data for the statistical analysis provided in Table 2, where the root-mean-square (RMS) force was calculated for each case. The mean force and its standard deviation (SD) are provided related to the confidence interval to be able to use for validation purposes in the following section. The uncertainty in the measurements of the tests was also examined by computing the coefficient of variation (COV). The results with the SD of 0.77 N and COV of 12.40% show that reasonable consistency was observed with relatively small variability.

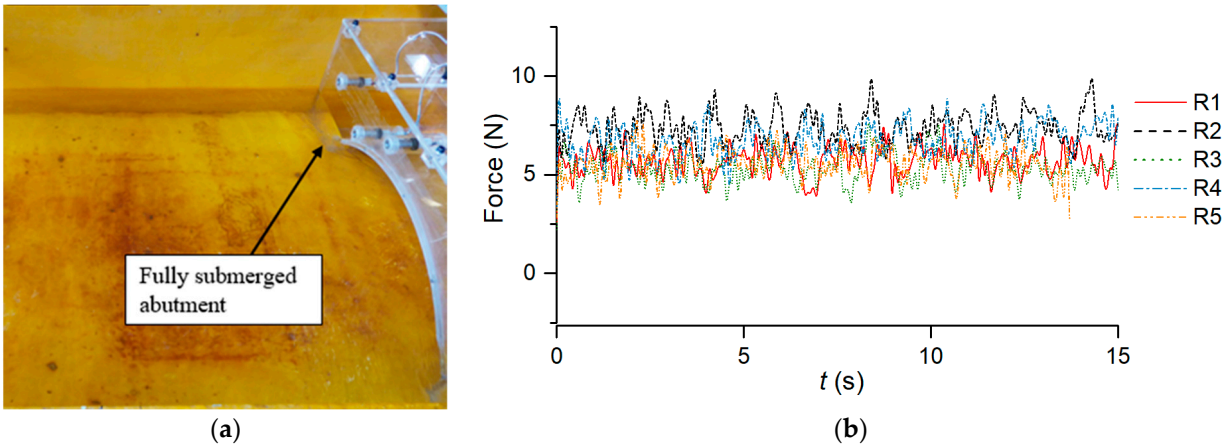

Figure 7. (**a**) Fully submerged abutment and (**b**) force–time histories in case 1, readings R1–R5.

Table 2. Test results in case 1.

Reading No.	$Force_{RMS}$ (N)
R1	5.74
R2	7.39
R3	5.40
R4	6.78
R5	5.62
Mean	6.19
SD	0.77
COV, %	12.40

Figure 8a–e shows the snapshots from debris motion records in millisecond precision to estimate the debris velocity at the impact in case 2. The debris velocity was estimated according to its travelling time between these specific distances; thus, the debris velocity was calculated as 0.291 m/s and 0.331 m/s based on 0.3 m and 0.1 m distances, see Figures 5b and 8a–e. Considering the increase in debris velocity close to the bridge, the 0.1 m distance was hereby used and relatively low COV was obtained (Table 3). The force–time histories are shown in Figure 9, the force including both hydrodynamic and debris impact load ranged between 32.94 N and 43.92 N, compared to the mean force obtained without debris of 6.19 N in case 1. The mean measured force with debris impact was therefore 6.25 times larger than the case without debris, equating to 6.25 times higher load. The impact durations in readings R1–R5 were obtained with 0.064 s, 0.081 s, 0.061 s, 0.087 s and 0.052 s. The SD and COV in the peak value of the debris impact were 4.00 N and 10.30%, respectively (Table 3).

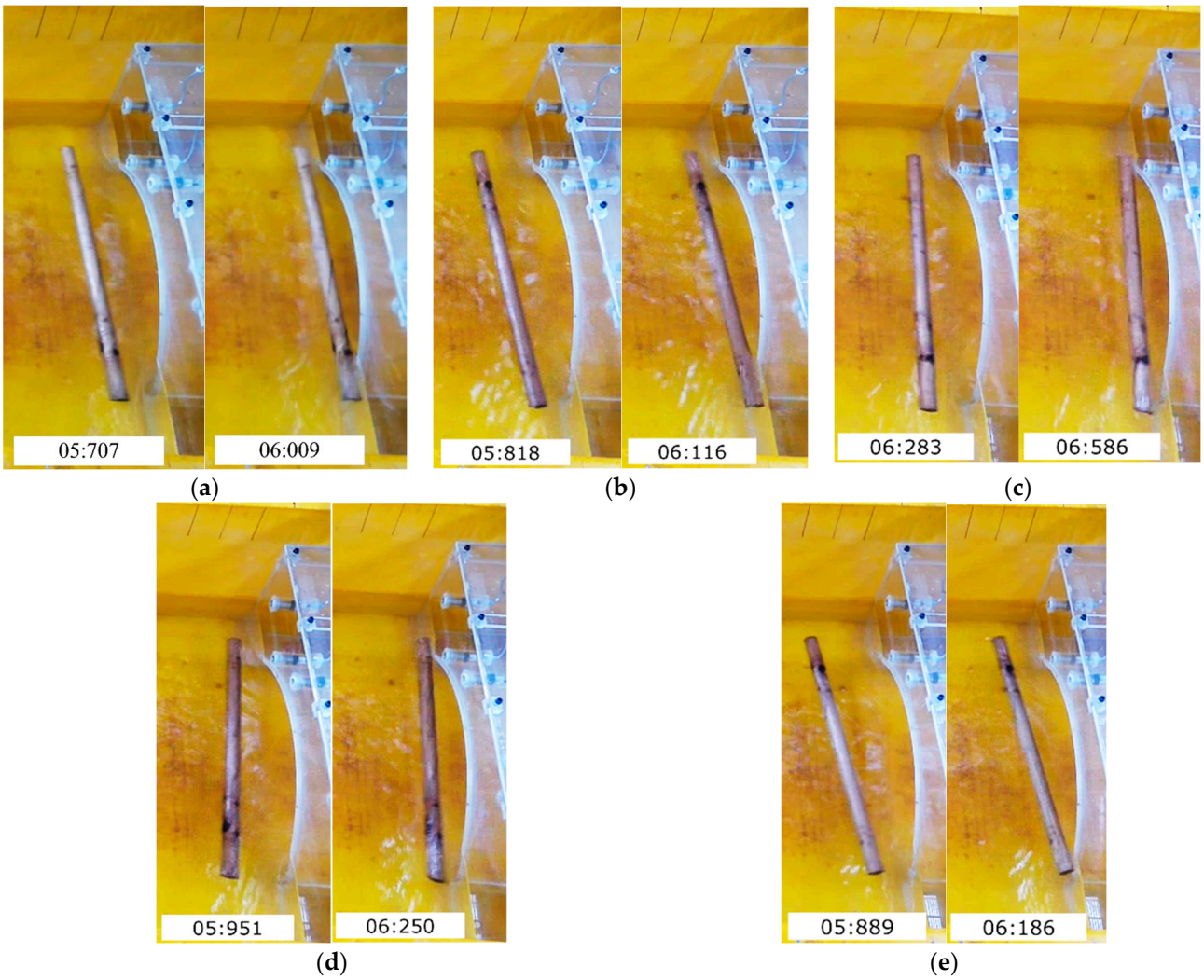

Figure 8. Motion of debris in case 2, (**a**–**e**) from readings R1–R5.

Table 3. Test results in case 2.

Reading No.	$Force_{Peak}$ (N)	u_{Debris} (m/s)
R1	32.94	0.331
R2	43.92	0.336
R3	35.25	0.330
R4	40.40	0.334
R5	40.84	0.337
Mean	38.67	0.334
SD	4.00	0.003
COV, %	10.33	0.818

In general, Figure 9 shows that there was not a clearly defined force–time impact profile. However, each run had some common characteristics. Before the largest measured force of the impact event, there was a short drop in the measured force (of different magnitude in each run). Then, there was a rapid rise to the peak impact force. After the peak impact force, there was a second drop in the force before a secondary impact force was measured. These dual peaks were due to differences in the debris orientation at impact compared to the initial orientation, whereby the long axis was parallel to the bridge span.

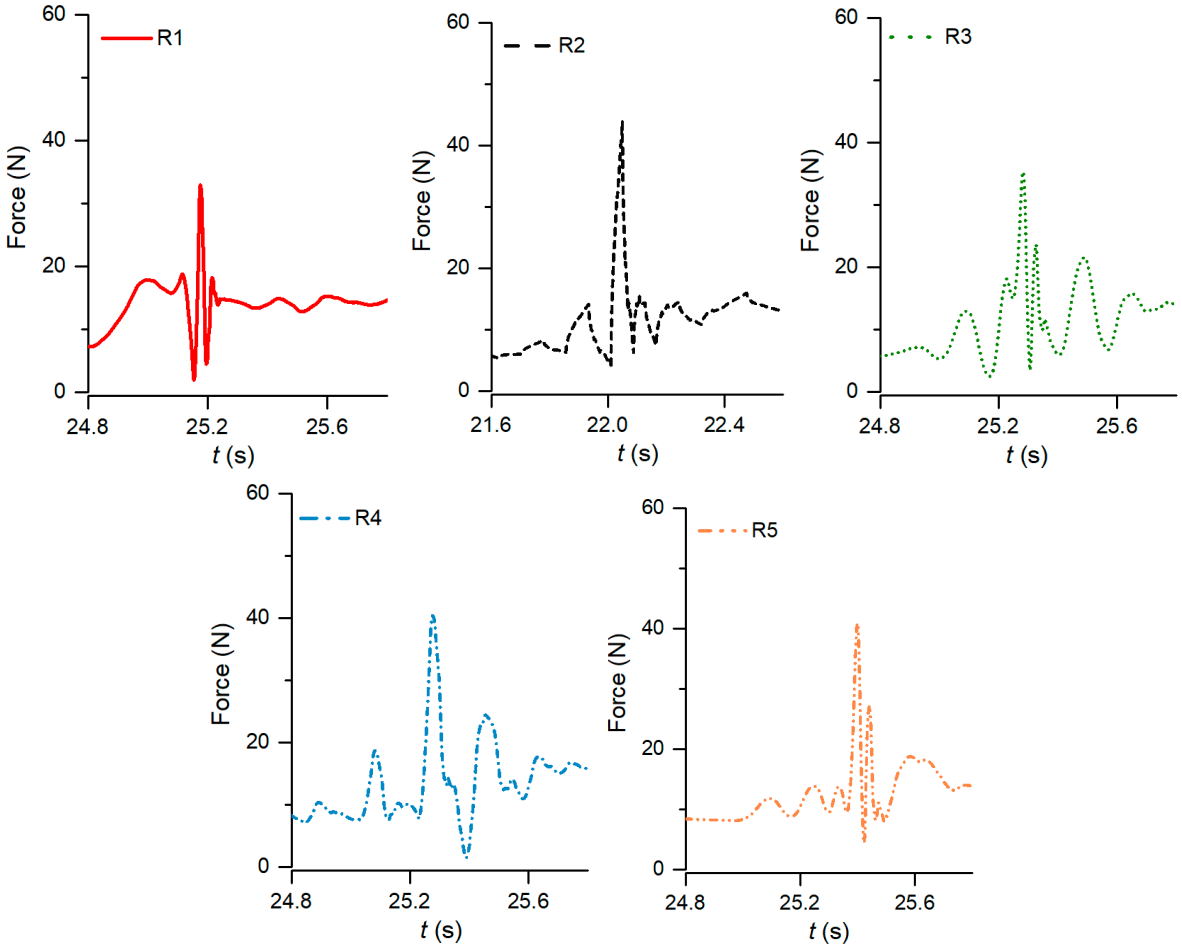

Figure 9. Force–time history at the debris impact, readings R1–R5.

3. Numerical Investigation: Smoothed Particle Hydrodynamics (SPH)

3.1. Numerical Setup

The smoothed particle hydrodynamics (SPH) method is employed in this study. The SPH theory, preliminary numerical setup, SPH parameters and GPU specifications used in the simulation and validation have been presented in detail by Majtan et al. [6]. The plan and side views of the numerical domain are given in Figure 10, where the inlet and outlet represent the V1 and V9 locations, respectively, in relation with the test area as well as computational efficiency. Following the experiment, a parabolic velocity profile with a free-surface velocity of 0.2 m/s and associated water depth were defined at the inlet, while water depth and constant velocity profile were imposed, considering the water depth measured at location V9 in the experiments and conservation of mass between these two locations. Note that the velocity profile measured at the location V9 was at the centreline of the flume width, which was not imposed at the outlet, considering its highest velocity value along location V9 and mass conservation. Note that the density was extrapolated at both the inlet and outlet. Considering recent development on the boundary conditions, the flume walls and bridge were created using the modified dynamic boundary condition (mDBC) rather than a dynamic boundary condition (DBC), while, due to limitations of the DualSPHysics code, the DBC was used for the floating object associated with available code in DualSPHysics v5.0 [64]. It should be emphasised that the main advantage of using mDBC in this research is to obtain pressure values on the structure without consideration of 1.5–2.0 h gap between solid and fluid particles [65,66], where h is the characteristic smoothing length. Since this gap size varies at each problem with each particle resolution, an accurate location needs to be defined to take pressure measurements.

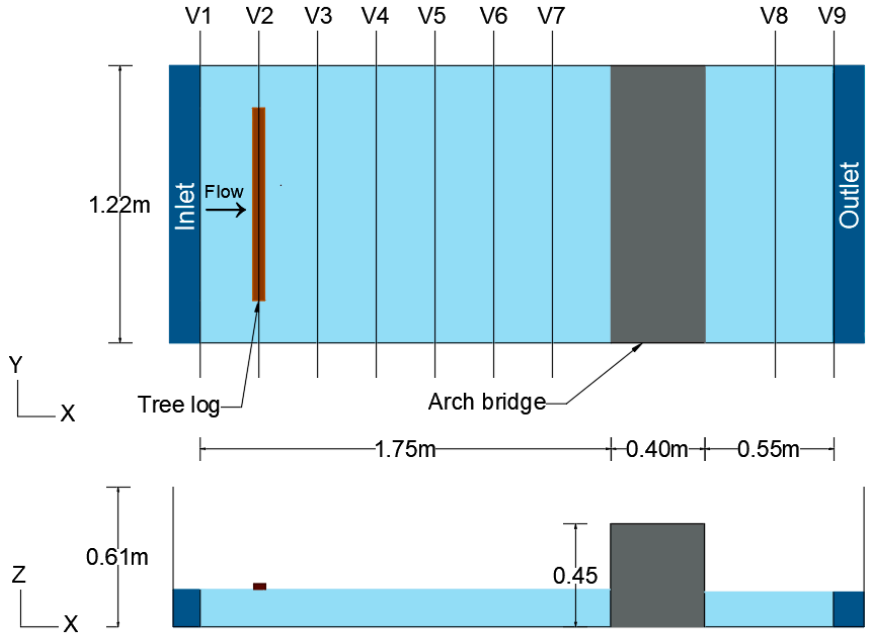

Figure 10. Plan and side views of the numerical domain with the velocity and water depth measurement locations of V1–V9 (not to scale).

Although a detailed convergence study was provided based on both hydrostatic and hydrodynamic loads for preliminary results in the study of Majtan et al. [6], a convergence study was performed for case 1 to ensure sufficient model resolution with a new boundary condition. Although the dimensions of the impacted structure as well as debris needs to be a multiple of *dp* in DualSPHysics, three different particle resolutions were used considering the shortest dimension of the impacted bridge in case 1 without the presence of the debris: 0.02 m, 0.01 m and 0.005 m. All simulations were run for 15 s physical time. The drag force–time history is given in Figure 11, where the experimental result in reading R1 is presented. As can be seen in the results, decreasing the *dp* from 0.02 m to 0.01 m improved the accuracy significantly by decreasing the error from 38.29% to 17.61% based on the mean force of 6.19 N obtained in the experiment, while a slight increase was obtained in the accuracy using 0.005 m *dp* corresponding to 4.2 times more total particles in the numerical domain, and 7.5 times longer computational time compared to those with the *dp* of 0.01 m, as shown in Table 4. To optimise the model resolution, a particle size of 0.01 m was used in all simulations. Note that although decreasing the size of numerical domain compared to the preliminary study, using mDBC increased the total particles in the simulation.

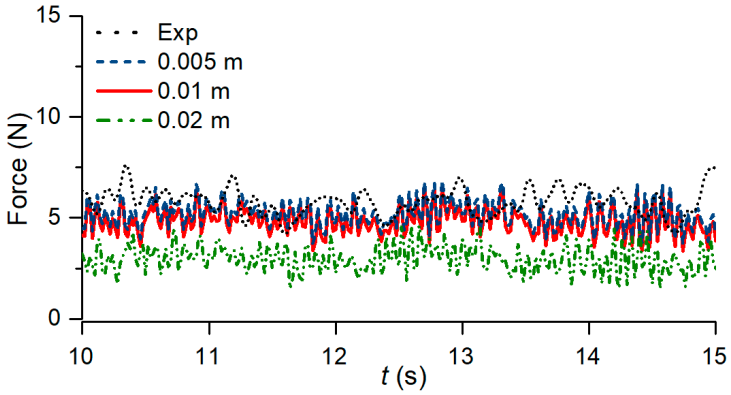

Figure 11. Force–time history on the bridge with different particle resolution vs experimental result in case 1, reading R1.

Table 4. Details of particle size convergence.

Flow Depth at V1 (m)	Particle Size, *dp* (m)	$Force_{RMS}$ (N)	Error (%)	Total Particle	Total Run Time
0.208	0.005	5.25	15.19	7,931,232	21 h 13 min
0.208	0.01	5.10	17.61	1,873,208	2 h 49 min
0.208	0.02	3.82	38.29	348,336	23 min

3.2. Validation of the SPH Model

3.2.1. Case 1: Hydrodynamic Load Only

Figure 12 shows the velocity distribution at the end of the simulation upstream and downstream of the bridge in case 1 with a fully submerged abutment. It can be seen that the water height was slightly higher upstream of the bridge and velocity values increased significantly along the bridge span. Figure 13a,b illustrates the water level elevation and depth-averaged velocity profile in the *x* direction at the centreline of the flume in case 1. The physical properties (water depth and velocity) at the V1 and V9 locations were defined at the inlet and outlet, while these properties obtained at the V2–V8 locations were compared herein. The flume was perfectly horizontal without any slope. To obtain the desired velocity and water level elevation at V1, the weir height was adjusted. Due to the presence of the weir at the outlet close to the bridge with lower water level compared to that at the inlet, the water level elevation decreased in the *x* direction along the flume in the experiment. In the numerical model with a horizontal flume bed and different water depth imposed at the inlet and outlet, the flow depth was slightly higher in the SPH model, with a maximum error of 2.42%, and associated depth-averaged velocity was lower, with a maximum error of 11.52%. The drag force in case 1 (Figure 13c) was obtained with 17.61% error, compared to the mean RMS force of 6.19 N in the experiment.

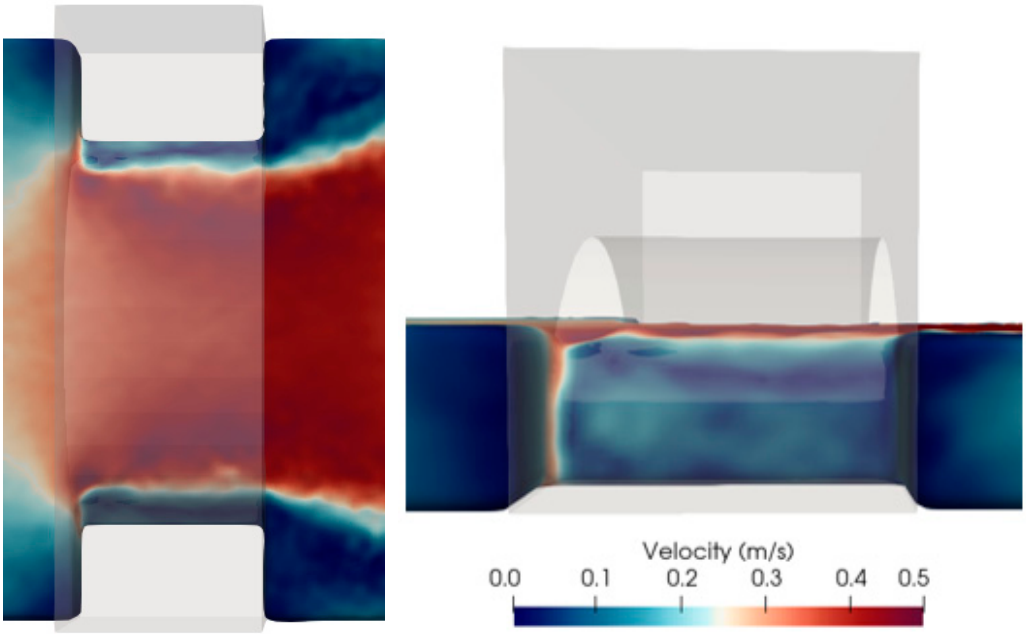

Figure 12. Plan view (**left**) and side view (**right**) with the velocity distribution and water depth upstream and downstream of the bridge.

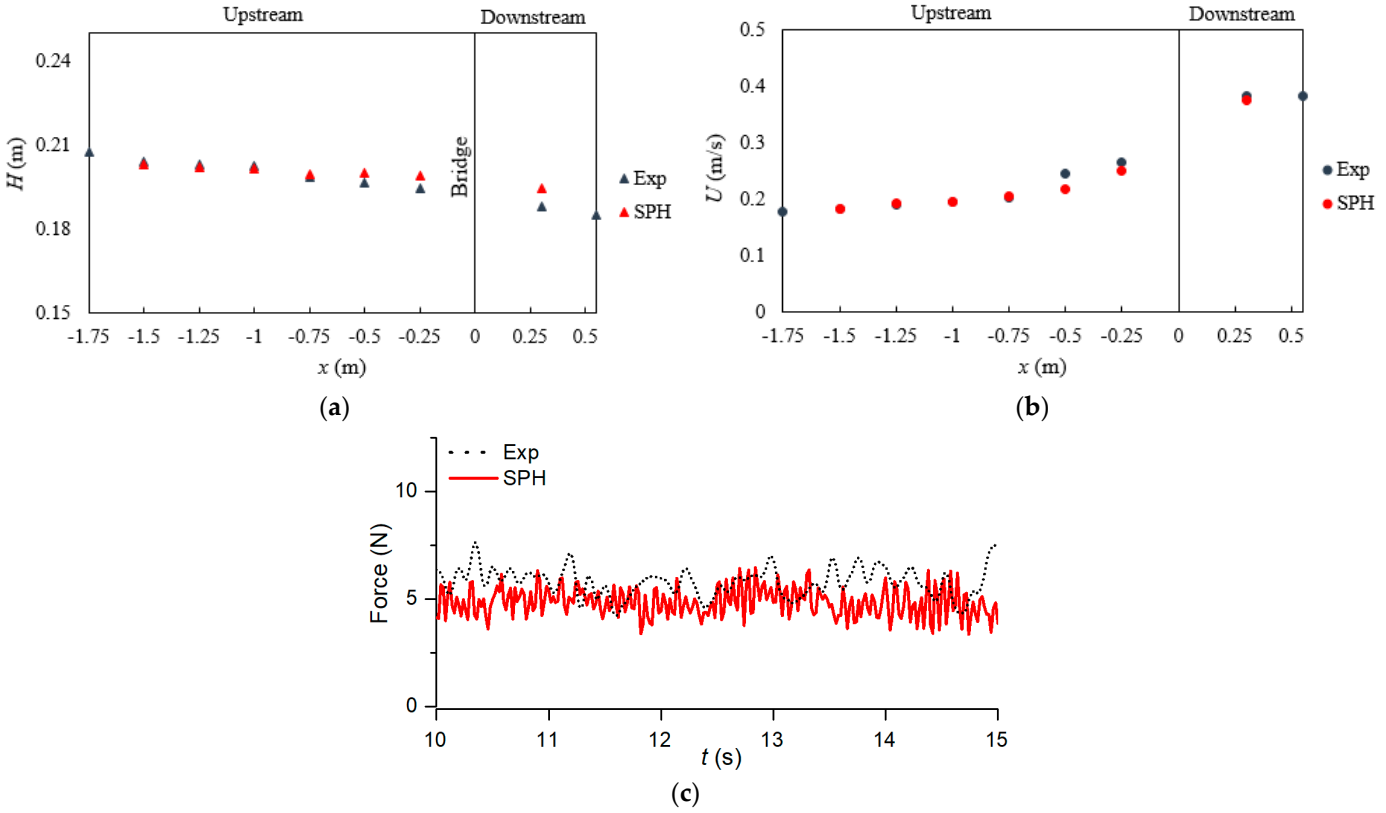

Figure 13. Comparison of SPH vs. experiment (**a**) water level elevation, (**b**) depth-averaged velocity profile in the x direction at the centreline of the flume and (**c**) force–time history in case 1, reading R1.

3.2.2. Case 2: Hydrodynamic and Debris Impact Loads

Figure 14a gives the debris velocity–time history in the flow direction (x) obtained in the SPH model where the debris was released inside the flow after the flow reached the same steady-state flow condition as the experiment, t = 4 s, while the debris was transported by the flow between t = 4 s and 7.026 s and then impacted the bridge with a velocity of 0.285 m/s. Thus, the SPH model predicted the debris velocity at impact with a 14.67% error based on the mean value of 0.334 m/s in the experiment, while the debris transport in the flow needs to be obtained in future experimental studies for detailed comparison. Figure 14b shows a comparison of the force–time history in the SPH and experiment in case 2, referring to reading R2, where the time refers to the experiment. The snapshots at the impact in the experiment (reading R1) and SPH model are given in Figure 14c,d, respectively. The impact duration of debris-induced force was higher in the SPH model, with 0.092 s against the mean of 0.069 s in the experiment. The SPH model predicted the peak force 5.84% higher, compared to the reading R2 in the experiment, and 16.81% against a mean value of 38.67 N, where the sampling frequency of 500 Hz was used based on the experimental results and the Nyquist–Shannon sampling theorem. This error might be due to the debris orientation at the impact and/or the assumption of the rigid body for both debris and bridge without consideration of their responses. It should be noted that different approaches are available in DualSPHysics v5.0 to consider the stiffness of the debris and bridge, as well as the interaction modelling between them. However, the wider research (within which this work forms a part) aims to achieve one-way coupling without consideration of bridge response, since these SPH outputs are used in another model as input loads to investigate the structural response of the bridge, as discussed in the following section. In a real-life masonry arch bridge, the rigid body assumption is reasonable given the stiffness of the bridge, particularly in the direction of flow.

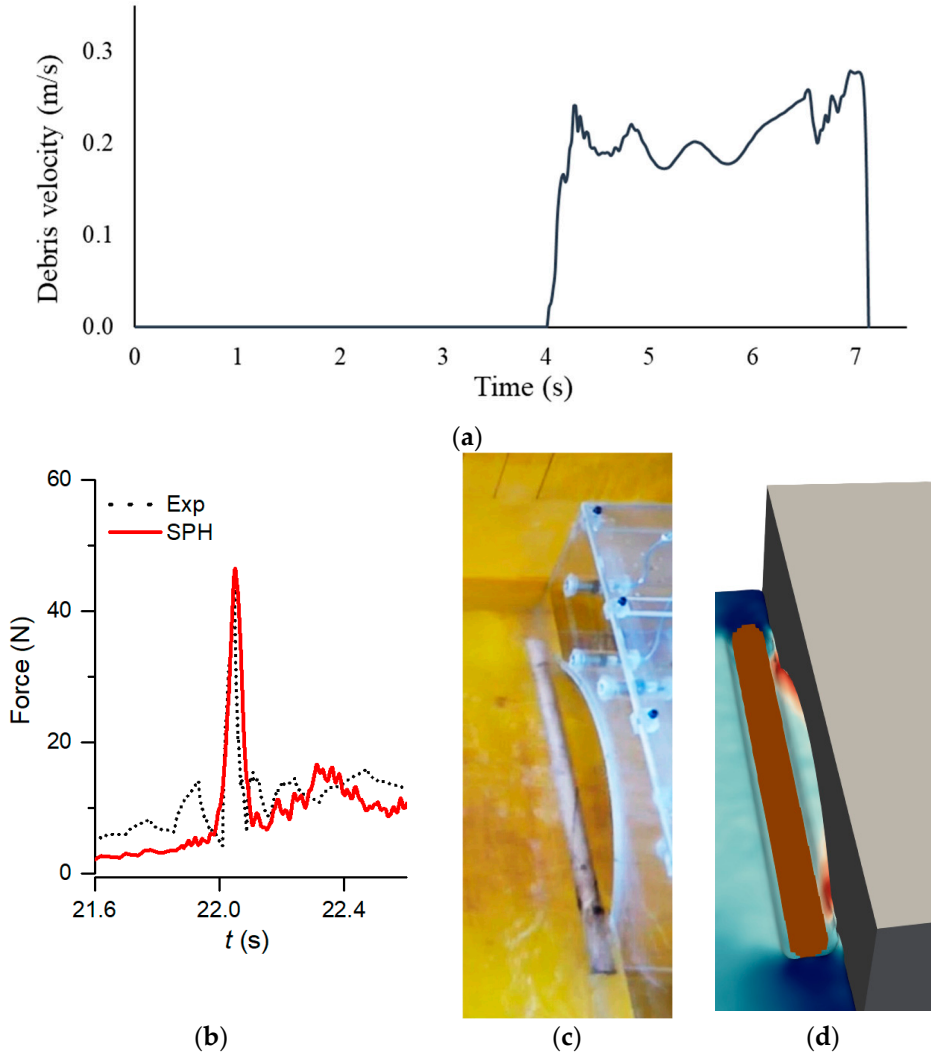

Figure 14. (**a**) Debris velocity–time history until the impact, (**b**) force–time history obtained in the SPH model vs. experiment (reading R2), (**c**) debris orientation at impact in the experiment (reading R1) and (**d**) SPH model in case 2.

3.3. Further Investigation: Pressure–Time Histories

3.3.1. Case 1: Hydrodynamic Load Only

Figure 15a,b illustrates velocity and pressure distributions on the 1:10 scale bridge in case 1 at the end of simulation with the presence of the free surface. As can be predicted, the maximum velocity occurred in the vicinity of the arch barrel close to the free surface, and the total pressure was highest at the bottom of the front spandrel wall of the arch bridge. To obtain averaged pressure histories based on pressure contour distribution on the upstream (front) and downstream (back) spandrel walls for investigating the structural response to this load, the measurement points given in Table 5 were used. The averaged pressure values obtained at these measurement points are shown in Figure 15c,d. It should be emphasised that these pressure values were observed on the scaled bridge.

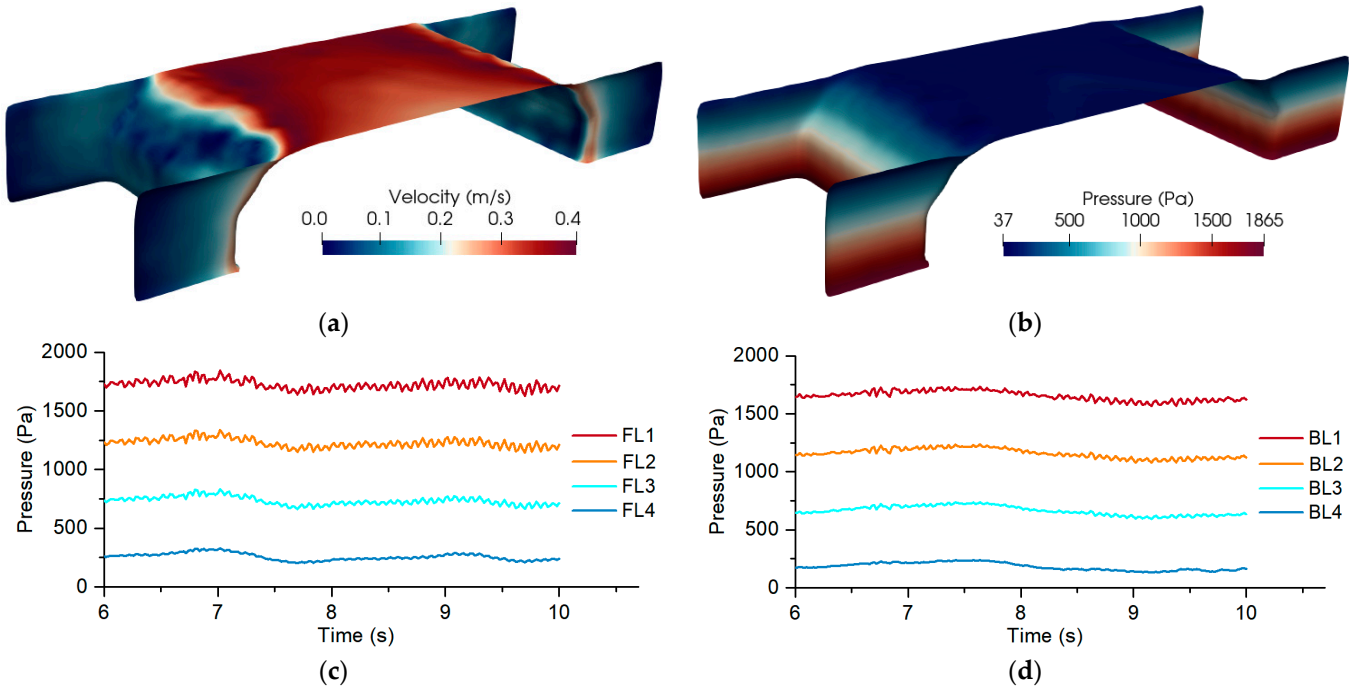

Figure 15. (**a**) Velocity and (**b**) pressure distributions on the bridge, (**c**) pressure–time histories on front and (**d**) back spandrel walls in case 1.

Table 5. Measurement points on front and back spandrel walls in case 1.

Front (F)		Back (B)	
Name	**Measurement Point (*x*,*y*,*z*)**	**Name**	**Measurement Point (*x*,*y*,*z*)**
FL1	1.75, 0.2, 0.03	BL1	2.15, 0.2, 0.03
FL2	1.75, 0.2, 0.08	BL2	2.15, 0.2, 0.08
FL3	1.75, 0.2, 0.13	BL3	2.15, 0.2, 0.13
FL4	1.75, 0.2, 0.18	BL4	2.15, 0.2, 0.18

3.3.2. Case 2: Hydrodynamic and Debris Impact Loads

To capture detailed debris-induced pressures on the bridge, numerical measuring probes were placed with spacing 0.02 m on the bridge front at x = 1.74 m, considering the gap between the debris and bridge associated with using DBC for the floating object. Figure 16a,b shows flow velocity and pressure distributions on the scaled bridge in case 2 when the debris impact was observed at t = 7.026 s. Compared to case 1, the presence of debris upstream of the bridge resulted in an increase in the free-surface velocity in the vicinity of the arch barrel close to the upstream side. Although the water pressure on the bridge slightly increased to 1883.1 Pa, a negative water pressure with a maximum value of 221.1 Pa occurred at the upstream spandrel wall with the debris impact. As shown in Figure 16c, a maximum pressure of 33,084 Pa was observed when the debris impacted the bridge at t = 7.026 s. Detailed pressure–time histories are provided in Figure 16d,e. Herein, (i) LP and RP are used to refer to the left- and right-hand sides, respectively, of the upstream bridge face impacted by the debris; and (ii) the numbers 1–5 indicate the numerical pressure probe impacted, with 1 being the furthest from the arch barrel and 5 being nearest the arch barrel. The rise times of the debris-induced pressure at the first impact ranged between 0.018 s and 0.024 s with the total impact duration of ~0.052 s (see Figure 16d,e), which was shorter than the total impact duration of debris-induced forces (see Figure 14b).

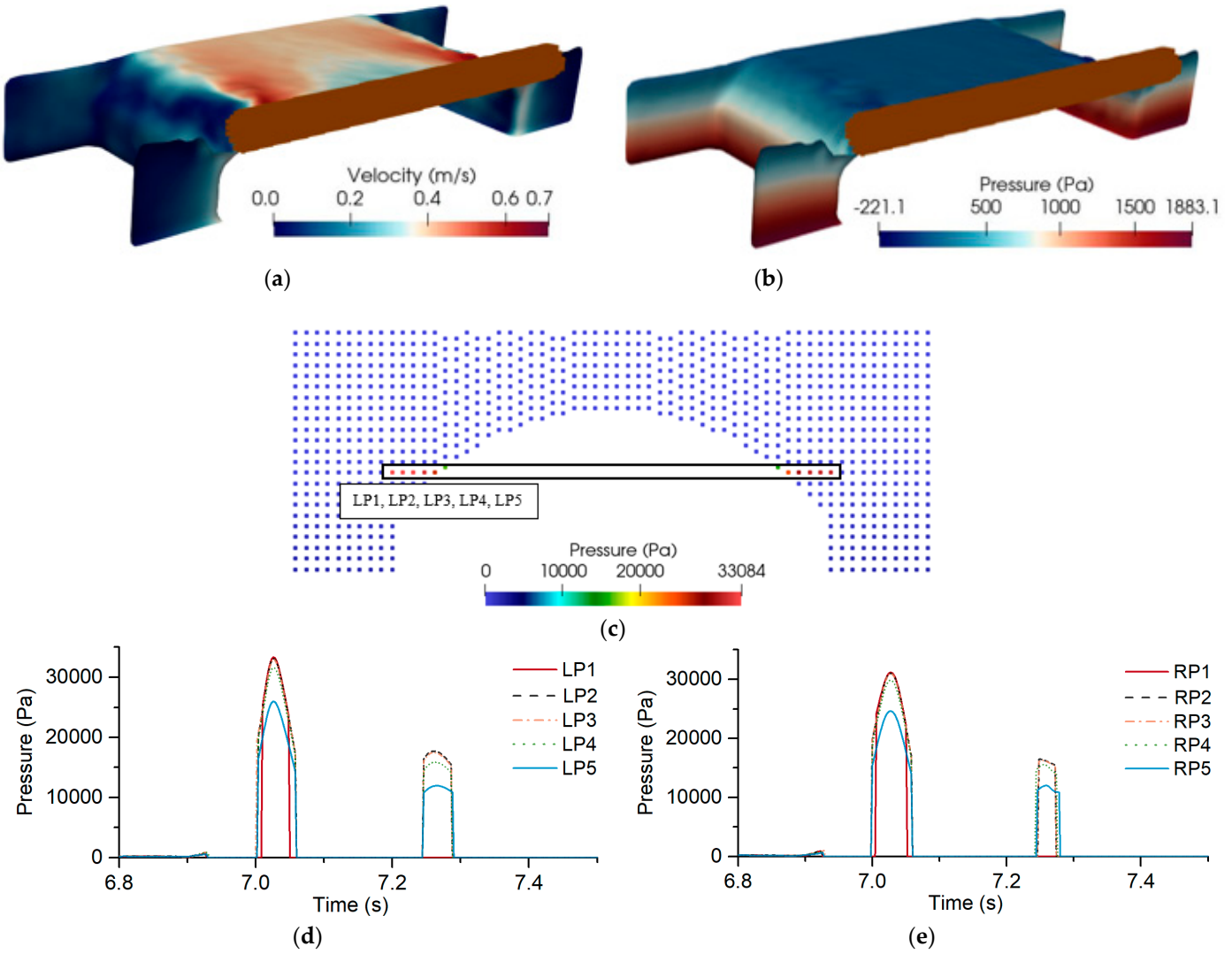

Figure 16. (**a**) Velocity and (**b**) pressure distributions on the bridge, (**c**) peak impact locations associated with the debris at t = 7.026 s in case 2 where the debris impact locations were numbered at the left (L) side of the bridge, (**d**) pressure–time histories at peak debris impact locations at left (L) side with LP1–LP5 and (**e**) at right (R) with RP1–RP5 between t = 6.8 s and t = 7.5 s.

4. Conclusions and Discussions

This paper is the first study in the open literature investigating, experimentally and numerically, the hydrodynamic and discrete floating debris impact loads on the superstructure of masonry arch bridges. The experimental investigation focusing on a representative single span arch bridge was first presented for the case of a fully submerged abutment. The main findings showed that the debris impact load was 6.25 times higher than the combination of hydrostatic and hydrodynamic loads for the case of no debris, with a mean debris impact duration of 0.069 s. Detailed statistical analyses were performed for each case in order to examine the repeatability as well as the uncertainty in the experiment. The COV was relatively low in the drag force, debris velocity and debris-induced peak force. It is expected that the COV could be further reduced by using an accelerometer to improve accuracy of measurement of the debris velocity. Special attention was devoted to defining the confidence intervals so as to examine the capability of the corresponding SPH model to simulate this type of fluid–structure and structure–structure interaction.

The SPH model successfully predicted the kinematics observed in the experiment. The depth-averaged velocity was obtained with a maximum error of 11.52%, and a maximum error of 2.42% was returned for the water surface elevation results. The hydrodynamic load

on the arch bridge had a 17.61% error compared to the mean RMS force of 6.19 N in the experiment. At the point of impact in the experiment, the debris orientation was not always perfectly at 0 degrees; this may account for some of the % error between the numerical and experimental results. The debris velocity was predicted with a 14.67% error at the impact based on the mean values of 0.334 m/s in the experiment. The SPH model provided a good agreement with the reading R2 in terms of the peak force with a 5.84% error, which was 16.81% considering the mean peak value in the experiment.

Using the validated SPH model, pressure–time histories across the entire surface of the bridge were generated. The results showed that the debris induced significant localised pressures on the bridge superstructure around the free-surface level equating to 165 times higher pressure compared to the corresponding case with no debris, i.e., hydrodynamic pressure alone. As highlighted, the combination of hydrodynamic and hydrostatic pressures at the upstream spandrel wall is expected to be higher than that at the downstream spandrel wall during real-life floods which can lead to a significant overturning force acting on the bridge. Investigation of the resulting forces, as well as the bridge response to these loads, will be detailed in the forthcoming publication.

These findings reveal that flood-induced loads without debris can be significant; however, the introduction of debris greatly increases the potential force generated. Floating debris impact resulted in peak forces of up to 6 times those generated by corresponding flows without debris. This clearly has implications for the global behaviour of the bridge superstructure. Similarly, the very high localised pressures predicted by the SPH model underline the vulnerability of certain parts of the masonry structure to damage, for example, in areas of the spandrel wall where isolated wash-out of fill may have occurred. Considering the lack of detailed assessment strategies for flood-induced loads on the superstructure of masonry arch bridges, this loading type and associated effects need to be understood to ensure the continued service of these bridge types.

Author Contributions: Conceptualization, E.M., L.S.C. and B.D.R.; methodology, E.M., L.S.C. and B.D.R.; validation, E.M.; formal analysis, E.M.; investigation, E.M., L.S.C. and B.D.R.; resources, E.M., L.S.C. and B.D.R.; data curation, E.M.; writing—original draft preparation, E.M.; writing—review and editing, E.M., L.S.C. and B.D.R.; visualization, E.M.; supervision, E.M., L.S.C. and B.D.R.; project administration, E.M., L.S.C. and B.D.R.; funding acquisition, E.M. All authors have read and agreed to the published version of the manuscript.

Funding: This research was funded by the Ministry of National Education of the Republic of Turkey.

Institutional Review Board Statement: Not applicable.

Informed Consent Statement: Not applicable.

Data Availability Statement: The experimental and numerical data provided in this study are available from the corresponding author by reasonable request.

Acknowledgments: The authors are grateful to Gregory Lane-Serff for providing some equipment used in this study, as well as technical staff, Robert Brown, William Storey and Kevin Totton for their assistance on the experimental works. Thanks are also due to Nicholas Omoding, Alejandro J. C. Crespo and Aaron English for invaluable discussions related to this research.

Conflicts of Interest: The authors declare no conflict of interest.

References

1. Hamill, L. *Bridge Hydraulics*; E & FN Spon: London, UK, 1999.
2. Proske, D. *Bridge Collapse Frequencies versus Failure Probabilities*; Springer: Berlin/Heidelberg, Germany, 2018; ISBN 3319738321.
3. Štulc, J. The 2002 Floods in the Czech Republic and their Impact on Built Heritage. *Herit. Risk* **2015**, 133–138. [CrossRef]
4. Xia, J.; Teo, F.Y.; Falconer, R.A.; Chen, Q.; Deng, S. Hydrodynamic experiments on the impacts of vehicle blockages at bridges. *J. Flood Risk Manag.* **2018**, *11*, S395–S402. [CrossRef]
5. Padgett, J.; Desroches, R.; Nielson, B.; Yashinsky, M.; Kwon, O.-S.; Burdette, N.; Tavera, E. Bridge Damage and Repair Costs from Hurricane Katrina. *J. Bridg. Eng.* **2008**, *13*, 6–14. [CrossRef]

6. Majtan, E.; Cunningham, L.S.; Rogers, B.D. Flood-induced Hydrodynamic and Debris Impact Forces on Single-span Masonry Arch Bridge. *J. Hydraul. Eng.* **2021**, *147*, 04021043. [CrossRef]
7. Orbán, Z. UIC Project on assessment, inspection and maintenance of masonry arch railway bridges. In Proceedings of the 5th International Conference on Arch Bridges, Madeira, Portugal, 12–14 September 2007; Volume 7, pp. 3–12.
8. Proske, D.; van Gelder, P. *Safety of Historical Stone Arch Bridges*; Springer: Berlin/Heidelberg, Germany, 2009; ISBN 9783540776161.
9. Proske, D.; Hubl, J. Historical arch bridges under horizontal loads. In Proceedings of the 5th International Conference on Arch Bridges, Madeira, Portugal, 12–14 September 2007; Volume 100.
10. *BD 97/12*; The Assessment of Scour and Other Hydraulic Actions at Highway Structures. National Highways: London, UK, 2012; Volume 3.
11. Takano, H.; Pooley, M. New UK guidance on hydraulic actions on highway structures and bridges. *Proc. Inst. Civ. Eng. Bridg. Eng.* **2021**, *174*, 231–238. [CrossRef]
12. Diehl, T.H. *Potential Drift Accumulation at Bridges*; US Department of Transportation, Federal Highway Administration, Research and Development, Turner-Fairbank Highway Research Center: McLean, VA, USA, 1997.
13. Parola, A.C.; Apelt, C.J.; Jempson, M.A. *NCHRP Report 445: Debris Forces on Highway Bridges*; Transportation Research Board (TRB), National Research Council: Washington, DC, USA, 2000.
14. *CD 356*; Design of Highway Structures for Hydraulic Action. National Highways: London, UK, 2020.
15. *AS5100.2:2017*; Bridge Design Loads. Australian Standard: Sydney, NSW, Australia, 2017; Volume 4.
16. May, R.W.P.; Ackers, J.C.; Kirby, A.M. *Manual on Scour at Bridges and Other Hydraulic Structures (C742)*; Ciria: London, UK, 2017; ISBN 0860175510.
17. FHWA. *Hydrodynamic Forces on Inundated Bridge Decks*; FHWA: Washington, DC, USA, 2009.
18. Robertson, I.N.; Riggs, H.R.; Yim, S.C.; Young, Y.L. Lessons from Hurricane Katrina Storm Surge on Bridges and Buildings. *J. Waterw. Port Coast. Ocean. Eng.* **2007**, *133*, 463–483. [CrossRef]
19. Ettema, R.; Arndt, R.; Roberts, P.; Wahl, T. *Hydraulic Modeling: Concepts and Practice*; American Society of Civil Engineers: Reston, VA, USA, 2000; ISBN 0784404151.
20. Panici, D.; Kripakaran, P. Assessing and mitigating risks to bridges from large wood using satellite imagery. *Proc. Inst. Civ. Eng. Bridg. Eng.* **2021**, 1–11. [CrossRef]
21. Hasanpour, A.; Istrati, D.; Buckle, I. Coupled sph–fem modeling of tsunami-borne large debris flow and impact on coastal structures. *J. Mar. Sci. Eng.* **2021**, *9*, 1068. [CrossRef]
22. Haehnel, R.B.; Daly, S.F. Maximum Impact Force of Woody Debris on Floodplain Structures. *J. Hydraul. Eng.* **2004**, *130*, 112–120. [CrossRef]
23. Stolle, J.; Nistor, I.; Goseberg, N.; Petriu, E. Multiple Debris Impact Loads in Extreme Hydrodynamic Conditions. *J. Waterw. Port Coast. Ocean. Eng.* **2020**, *146*, 04019038. [CrossRef]
24. Andersson, B.; Andersson, R.; Håkansson, L.; Mortensen, M.; Sudiyo, R.; Van Wachem, B. *Computational Fluid Dynamics for Engineers*; Cambridge University Press: Cambridge, UK, 2011; Volume 9781107018, ISBN 9781139093590.
25. Istrati, D.; Buckle, I.G. *Tsunami Loads on Straight and Skewed Bridges—Part 2: Numerical Investigation and Design Recommendations*; Oregon Department of Transportation: Salem, OR, USA, 2021.
26. Zhu, M.; Elkhetali, I.; Scott, M.H. Validation of OpenSees for Tsunami Loading on Bridge Superstructures. *J. Bridg. Eng.* **2018**, *23*, 04018015. [CrossRef]
27. Xiang, T.; Istrati, D. Assessment of extreme wave impact on coastal decks with different geometries via the arbitrary lagrangian-eulerian method. *J. Mar. Sci. Eng.* **2021**, *9*, 1342. [CrossRef]
28. Shadloo, M.S.; Oger, G.; Le Touzé, D. Smoothed particle hydrodynamics method for fluid flows, towards industrial applications: Motivations, current state, and challenges. *Comput. Fluids* **2016**, *136*, 11–34. [CrossRef]
29. Erduran, K.S.; Seckin, G.; Kocaman, S.; Atabay, S. 3D numerical modelling of flow around skewed bridge crossing. *Eng. Appl. Comput. Fluid Mech.* **2012**, *6*, 475–489. [CrossRef]
30. Hartana; Murakami, K.; Yamaguchi, Y.; Maki, D. 2-Phase Flow Analysis of Tsunami Forces Acting on Bridge Structures. *J. Jpn. Soc. Civ. Eng. Ser. B3 Ocean. Eng.* **2013**, *69*, I_347–I_352. [CrossRef]
31. Chu, C.-R.; Chung, C.-H.; Wu, T.-R.; Wang, C.-Y. Numerical Analysis of Free Surface Flow over a Submerged Rectangular Bridge Deck. *J. Hydraul. Eng.* **2016**, *142*, 04016060. [CrossRef]
32. Ebrahimi, M.; Kahraman, R.; Kripakaran, P.; Djordjević, S.; Tabor, G.; Prodanović, D.M.; Arthur, S.; Riella, M. Scour and Hydrodynamic Effects of Debris Blockage at Masonry Bridges: Insights from Experimental and Numerical Modelling. In Proceedings of the 37th International Association for Hydro-Environment Engineering and Research (IAHR) Congress, Kuala Lumpur, Malaysia, 14–18 August 2017.
33. Nasim, M.; Setunge, S.; Zhou, S.; Mohseni, H. An investigation of water-flow pressure distribution on bridge piers under flood loading. *Struct. Infrastruct. Eng.* **2019**, *15*, 219–229. [CrossRef]
34. Oudenbroek, K.; Naderi, N.; Bricker, J.D.; Yang, Y.; van der Veen, C.; Uijttewaal, W.; Moriguchi, S.; Jonkman, S.N. Hydrodynamic and debris-damming failure of bridge decks and piers in steady flow. *Geosciences* **2018**, *8*, 409. [CrossRef]
35. Kahraman, R.; Riella, M.; Tabor, G.R.; Ebrahimi, M.; Djordjević, S.; Kripakaran, P. Prediction of flow around a sharp-nosed bridge pier: Influence of the Froude number and free-surface variation on the flow field. *J. Hydraul. Res.* **2019**, *1686*, 582–583. [CrossRef]

36. Benzi, R.; Succi, S.; Vergassola, M. The lattice Boltzmann equation: Theory and applications. *Phys. Rep.* **1992**, *222*, 145–197. [CrossRef]
37. Rothman, D.; Zaleski, S. *Lattice-Gas Cellular Automata: Simple Models of Complex Hydrodynamics*; Cambridge University Press: Cambridge, UK, 2004.
38. Shimizu, Y.; Gotoh, H.; Khayyer, A. An MPS-based particle method for simulation of multiphase flows characterized by high density ratios by incorporation of space potential particle concept. *Comput. Math. Appl.* **2018**, *76*, 1108–1129. [CrossRef]
39. Khayyer, A.; Gotoh, H.; Falahaty, H.; Shimizu, Y. An enhanced ISPH–SPH coupled method for simulation of incompressible fluid–elastic structure interactions. *Comput. Phys. Commun.* **2018**, *232*, 139–164. [CrossRef]
40. Colagrossi, A.; Landrini, M. Numerical simulation of interfacial flows by smoothed particle hydrodynamics. *J. Comput. Phys.* **2003**, *191*, 448–475. [CrossRef]
41. Oger, G.; Doring, M.; Alessandrini, B.; Ferrant, P. An improved SPH method: Towards higher order convergence. *J. Comput. Phys.* **2007**, *225*, 1472–1492. [CrossRef]
42. Liu, M.B.; Liu, G.R. Smoothed particle hydrodynamics (SPH): An overview and recent developments. *Arch. Comput. Methods Eng.* **2010**, *17*, 25–76. [CrossRef]
43. Marrone, S.; Colagrossi, A.; Antuono, M.; Colicchio, G.; Graziani, G. An accurate SPH modeling of viscous flows around bodies at low and moderate Reynolds numbers. *J. Comput. Phys.* **2013**, *245*, 456–475. [CrossRef]
44. Monaghan, J.J.; Rafiee, A. A simple SPH algorithm for multi-fluid flow with high densityratios. *Int. J. Numer. Methods Fluids* **2013**, *71*, 537–561. [CrossRef]
45. Zhao, T. Investigation of Landslide-Induced Debris Flows by the DEM and CFD. Ph.D. Thesis, University of Oxford, Oxford, UK, 2014; 251p.
46. Canelas, R.B.; Crespo, A.J.C.; Domínguez, J.M.; Ferreira, R.M.L.; Gómez-Gesteira, M. SPH-DCDEM model for arbitrary geometries in free surface solid-fluid flows. *Comput. Phys. Commun.* **2016**, *202*, 131–140. [CrossRef]
47. Capasso, S.; Tagliafierro, B.; Martínez-Estévez, I.; Domínguez, J.M.; Crespo, A.J.C.; Viccione, G. A DEM approach for simulating flexible beam elements with the Project Chrono core module in DualSPHysics. *Comput. Part. Mech.* **2022**, 1–17. [CrossRef]
48. Khayyer, A.; Tsuruta, N.; Shimizu, Y.; Gotoh, H. Multi-resolution MPS for incompressible fluid-elastic structure interactions in ocean engineering. *Appl. Ocean Res.* **2019**, *82*, 397–414. [CrossRef]
49. Istrati, D.; Buckle, I.G. Effect of Fluid-Structure Interaction on Connection Forces in Bridges due to Tsunami Loads. In Proceedings of the 30th US-Japan Bridge Engineering Workshop, Washington, DC, USA, 21 October 2014; pp. 21–23.
50. Al-Faesly, T.Q.; Nistor, I.; Palermo, D.; Cornett, A. Experimental study of structures subjected to hydrodynamic and debris impact forces. In Proceedings of the Annual Conference of the Canadian Society for Civil Engineering, Montreal, QC, Canada, 29 May–1 June 2013; Volume 1, pp. 118–127.
51. Ducrocq, T.; Cassan, L.; Chorda, J.; Roux, H. Flow and drag force around a free surface piercing cylinder for environmental applications. *Environ. Fluid Mech.* **2017**, *17*, 629–645. [CrossRef]
52. Boothby, T.E.; Roberts, B.J. Transverse behaviour of masonry arch bridges. *Struct. Eng.* **2001**, *79*, 21–26.
53. Comiti, F.; Andreoli, A.; Lenzi, M.A.; Mao, L. Spatial density and characteristics of woody debris in five mountain rivers of the Dolomites (Italian Alps). *Geomorphology* **2006**, *78*, 44–63. [CrossRef]
54. Magilligan, F.J.; Nislow, K.H.; Fisher, G.B.; Wright, J.; Mackey, G.; Laser, M. The geomorphic function and characteristics of large woody debris in low gradient rivers, coastal Maine, USA. *Geomorphology* **2008**, *97*, 467–482. [CrossRef]
55. Ebrahimi, M.; Kripakaran, P.; Prodanović, D.M.; Kahraman, R.; Riella, M.; Tabor, G.; Arthur, S.; Djordjević, S. Experimental Study on Scour at a Sharp-Nose Bridge Pier with Debris Blockage. *J. Hydraul. Eng.* **2018**, *144*, 04018071. [CrossRef]
56. Heller, V. Scale effects in physical hydraulic engineering models. *J. Hydraul. Res.* **2011**, *49*, 293–306. [CrossRef]
57. Mathews, R.; Hardman, M. Lessons learnt from the December 2015 flood event in Cumbria, UK. *Proc. Inst. Civ. Eng. Forensic Eng.* **2017**, *170*, 165–178. [CrossRef]
58. Istrati, D.; Hasanpour, A.; Buckle, I.G. Numerical Investigation of Tsunami-Borne Debris Damming Loads on a Coastal Bridge. In Proceedings of the 17 World Conference on Earthquake Engineering, Sendai, Japan, 27 September 2020; pp. 1–12.
59. Jeffcoate, P. *Experimental and Computational Modelling of 3D Flow and Bed Shear Stresses Downstream from a Multiple Duct Tidal Barrage*; The University of Manchester: Manchester, UK, 2013; pp. 1–345.
60. Nortek, A.S. *The Comprehensive Manual for Velocimeters*; Nortek AS: Rud, Norway, 2018.
61. Ficker, T.; Martišek, D. 3D Image Reconstructions and the Nyquist–Shannon Theorem. *3D Res.* **2015**, *6*, 23. [CrossRef]
62. Robertson, I.N.; Riggs, H.R.; Mohamed, A. Experimental results of tsunami bore forces on structures. *Proc. Int. Conf. Offshore Mech. Arct. Eng.-OMAE* **2008**, *1*, 509–517. [CrossRef]
63. Istrati, D. Large-Scale Experiments of Tsunami Inundation of Bridges including Copyright by Denis Istrati 2017 All Rights Reserved. Ph.D. Thesis, University of Nevada, Reno, Nevada, 2017.
64. English, A.; Domínguez, J.M.; Vacondio, R.; Crespo, A.J.C.; Stansby, P.K.; Lind, S.J.; Chiapponi, L.; Gómez-Gesteira, M. Modified dynamic boundary conditions (mDBC) for general-purpose smoothed particle hydrodynamics (SPH): Application to tank sloshing, dam break and fish pass problems. *Comput. Part. Mech.* **2021**, 1–15. [CrossRef]

65. Pringgana, G.; Cunningham, L.S.; Rogers, B.D. Modelling of tsunami-induced bore and structure interaction. *Proc. Inst. Civ. Eng. Eng. Comput. Mech.* **2016**, *169*, 109–125. [CrossRef]
66. Baines, A.; Watson, P.; Cunningham, L.S.; Rogers, B.D.; Murphy, J.; Lizondo, S. Modelling shore-side pressure distributions from violent wave breaking at a seawall. *Proc. Inst. Civ. Eng. Eng. Comput. Mech.* **2019**, *172*, 118–123. [CrossRef]